Boundary layer analysis in turbulent Rayleigh-Bénard convection in air: Experiment versus simulation

Ling Li, Nan Shi, Ronald du Puits, Christian Resagk, Jörg Schumacher, and André Thess
Institut für Thermo- und Fluiddynamik, Technische Universität Ilmenau, Postfach 100565, D-98684 Ilmenau, Germany
(Received 3 April 2012; published 31 August 2012)

We report measurements and numerical simulations of the three-dimensional velocity and temperature fields in turbulent Rayleigh-Bénard convection in air. Highly resolved velocity and temperature measurements inside and outside the boundary layers have been directly compared with equivalent data obtained in direct numerical simulations (DNSs). This comparison comprises a set of two Rayleigh numbers at $\mathrm{Ra} = 3 \times 10^9$ and 3×10^{10} and a fixed aspect ratio; this is the ratio between the diameter and the height of the Rayleigh-Bénard cell of $\Gamma = 1$. We find that the measured velocity data are in excellent agreement with the DNS results while the temperature data slightly differ. In particular, the measured mean temperature profile does not show the linear trend as seen in the DNS data, and the measured gradients at the wall are significantly higher than those obtained from the DNS. Both viscous and thermal boundary layer thickness scale with respect to the Rayleigh number as $\delta_v \sim \mathrm{Ra}^{-0.24}$ and $\delta_\theta \sim \mathrm{Ra}^{-0.24}$, respectively.

DOI: 10.1103/PhysRevE.86.026315 PACS number(s): 47.27.te, 44.20.+b, 47.50.Ef

I. INTRODUCTION

A great variety of natural and technical turbulent flows is driven by temperature differences. Rayleigh-Bénard (RB) convection is one of the paradigmatic models to study the details of this kind of turbulence. In its simplest setting an infinitely extended fluid layer is enclosed by two isothermal plates: a hot plate at the bottom and a cold plate at the top. In experiments the finite flow volume is established by additional thermally insulated side walls, which can form a closed cylindrical cell. The focus of most experimental and numerical studies in this configuration is a better understanding of the mechanisms of turbulent heat transport [1,2]. Since nonpermeable walls enclose the moving fluid, boundary layers (BLs) do form for all turbulent fields involved. Although these BLs become ever thinner when the driving of the convective turbulence is increased, they cannot be neglected. The reason is that all the upward directed flux of heat which is provided from the isothermally heated bottom plate has to pass these tiny layers at the bottom and top. Furthermore, it is well-known that a large-scale circulation (LSC) builds up in closed cells, which also interacts with the boundary layers. A better understanding of the mechanisms of global turbulent heat transport at large Rayleigh numbers remains thus intimately connected with a better understanding of the physics inside the boundary layers.

Exactly this point is the main motivation of the present work: a joint experimental and numerical analysis and direct comparison of the structure of the BL of the velocity and temperature fields in a cylindrical turbulent Rayleigh-Bénard cell for convection in air at two Rayleigh numbers larger than $\mathrm{Ra} = 10^9$. In this paper we take a first step in this direction and compare the statistics of time series of the turbulent fields taken at points inside and outside the boundary layers, allowing us to compose wall-normal profiles of the three velocity components and temperature at a few different locations close to the cooling plate of the cell. Experimentally it requires a convection cell which is several meters high in order to take mean profiles in a less-than-a-centimeter-thick BLs, such as in the "Barrel of Ilmenau" (BOI) [3]. Numerically this enforces comprehensive direct numerical simulations (DNSs) in which the computational grid is fine enough to represent all structures in the boundary layers [4].

The dynamics of the turbulent flow in a RB cell is determined by three dimensionless parameters: the Rayleigh number $\mathrm{Ra} = (\alpha g \Delta\vartheta H^3)/(\nu\kappa)$, the Prandtl number $\mathrm{Pr} = \nu/\kappa$, and the aspect ratio $\Gamma = D/H$. In response to the sustained temperature difference a turbulent flow with a Reynolds number $\mathrm{Re} = \bar{v}H/\nu$ is established. This flow enhances the transport of heat far beyond the level that is achievable by thermal diffusion. The Nusselt number quantifies exactly this ratio and is defined as $\mathrm{Nu} = (4H\dot{Q})/(\lambda\pi D^2\Delta\vartheta)$. In these definitions variables stand for the following physical quantities: α is the isobaric expansion coefficient, g the gravitational acceleration, $\Delta\vartheta$ the temperature difference between both horizontal plates, ν the kinematic viscosity, κ the thermal diffusivity, D the diameter of the convection cell, H its height, and $\bar{v}$ the mean velocity. We denote $\dot{Q}$ as the convective heat flux and λ as the thermal conductivity.

Scaling theories of turbulent convection aim at predicting transport laws for heat, Nu(Ra, Pr), and momentum, Re(Ra, Pr). They require a physical model for the BLs as an input. While the theory by Shraiman and Siggia [5,6] builds on existing turbulent boundary layers close to the isothermal plates, Grossmann and Lohse [7,8] assumed a Prandtl-Blasius-type BL [9]. Our joint high-resolution BL analysis will allow us to compare our findings with the assumptions and provides a further motivation to the present work.

In the last few years a number of experiments have been performed in various fluids and gases aiming to study the temperature and the velocity field inside the BLs. Velocity and temperature profile measurements in water using laser Doppler anemometry (LDA) were reported in Qiu and Tong [10], who studied the LSC of the flow at $\mathrm{Ra} = 10^9$. Later Sun, Cheung, and Xia [11] and Zhou and Xia [12] studied the BL profiles by particle image velocimetry (PIV) for convection in water at $\mathrm{Pr} = 4.3$. They found that the Prandtl-Blasius solution is a good approximation for the velocity BL for Rayleigh numbers between 10^9 and 10^{10}. Their Cartesian convection cell was,

however, very narrow in the third direction such that the LSC is confined to a quasi-two-dimensional flow. BL measurements for convection in air up to a $\mathrm{Ra} = 10^{11}$ have been conducted with a two-component LDA measurement [13,14]. In these experiments deviations from the Prandtl-Blasius case were detected. Three aspects turn out to improve the agreement with the classical Prandtl-Blasius theory: the switch to a quasi-two-dimensional experiment or two-dimensional DNS that constrains the LSC, an increase in the Prandtl number, and a rescaling by an instantaneously defined BL thickness. All these directions in various combinations have been discussed in Refs. [12,15]. Recent DNSs for Rayleigh numbers up to 2×10^{12} found, however, that the differences grow for the BL profiles of the temperature field [16].

The outline of the paper is as follows. In Sec. II the experimental facility and the measurement technique is described. In Sec. III we summarize the DNS model. In Sec. IV we compare results of the mean velocity and temperature profiles and their fluctuations. We compare experimental data at $\mathrm{Ra} = 3.44 \times 10^9$, $\Delta T = 2.4$ K, with DNS data at $\mathrm{Ra} = 3 \times 10^9$. Furthermore, experimental data at $\mathrm{Ra} = 2.88 \times 10^{10}$, $\Delta T = 20$ K, can be compared with DNS data at $\mathrm{Ra} = 3 \times 10^{10}$. In this section we also include BL analysis from other experimental data records in order to discuss trends for the scaling of the BL thickness and shear Reynolds number in a range of Rayleigh numbers varying from $\mathrm{Ra} = 3.44 \times 10^9$ to 9.97×10^{11}. These studies are followed by investigations of the LSC, the mean angle of its rotation, and autocorrelation functions of the azimuthal angle. We summarize our work in Sec. V.

II. EXPERIMENT

All measurements were conducted in the BOI, a large-scale Rayleigh-Bénard experiment. It consists of a virtually adiabatic cylinder of $D = 7.15$ m filled with ambient air. It is heated from below and cooled from above by two plates with uniform temperature. The bottom plate consists of two parts: an electrical underfloor heating system embedded in a 5 cm floating screed layer and isolated to the ground with 0.3 m polyurethane plates and an overlay in which water circulates. The water circulation inside this overlay makes the temperature at the surface of the heating plate uniform and balances the various convective heat flux at the plate-air interface. Both layers are thermally coupled by a 2 mm silicon pad. The free-hanging cooling plate consists of 16 segments with an internal water circulation. The deviation of any local temperature at the surface of both plates from the global mean temperature was typically less than 0.5 K. Over the period of one measurement the mean surface temperature varies in a band of 0.02 K. A detailed description of the facility can be found in Refs. [13,14]. The lowest accessible Ra in this facility at aspect ratio one is $\mathrm{Ra}_{\mathrm{min}} = 5 \times 10^{10}$, which is larger than the maximum Rayleigh number in the numerical simulations, $\mathrm{Ra}_{\mathrm{sim}} = 3 \times 10^{10}$. In order to match the experimental parameters to those from the DNS for the case of $\Gamma = 1$, a cylindrical inset with a diameter of 2.5 m and a height of 2.5 m has been installed between the heating and the cooling plates. The smaller plexiglass cell is located inside the big barrel and is very well sealed by the upper cooling plate and lower heating plate. The surrounding environment of the smaller cell has the same temperature difference as the inside volume of the BOI. Thus no thermal exchange across the side walls is present, and the adiabatic side wall boundary condition is well established. Four windows are located at different positions of the cooling plate (see left panel of Fig. 1) permitting access for the optical device and temperature sensors.

A. Velocity measurement setup

We study the three-dimensional (3D) velocity field by combining a one-dimensional (1D) Nd-YAG-laser probe ($\lambda = 532$ nm) and a two-dimensional (2D) argon-ion-laser probe ($\lambda = 514.5$ nm, $\lambda = 488$ nm). Both make up the so-called FiberFlow-LDA system from Dantec Dynamics and work in the back-scattering mode. Figure 1(b) shows the arrangement of the probes above the cooling plate where a glass window permits the optical access to the boundary layer. This window

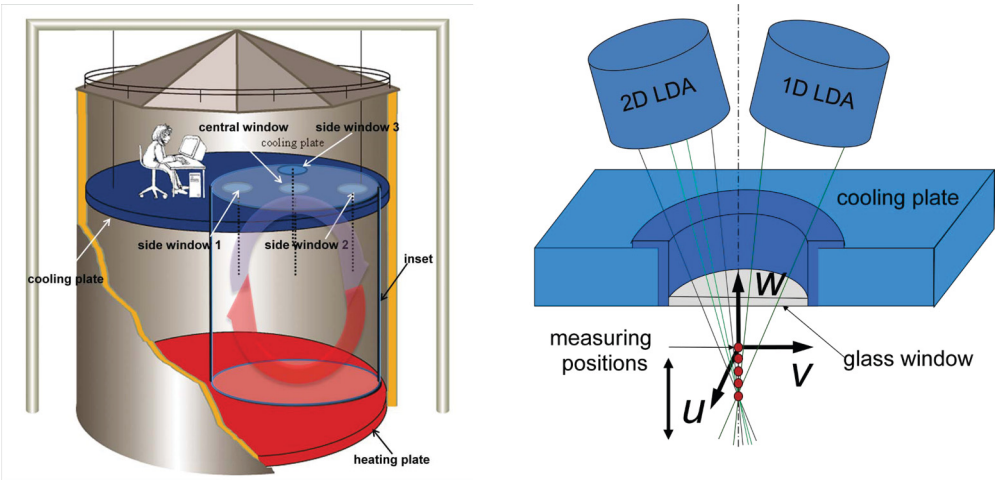

FIG. 1. (Color online) Description of the experiment. (a) Sketch of "Barrel of Ilmenau" with the new inset cell of 2.5 m height and 2.5 m diameter. In this paper we present the results at center and side window 1, 2, and 3. (b) Setup of the 3D-laser Doppler anemometry measurement, which is mounted above the cooling plate. u, v, and w are the desired velocity components in Cartesian coordinates.

is of good thermal conductivity and stuck into the cooling plate using a highly conducting adhesive. Thus, the temperature of the glass window is very close to the temperature of the cooling plate. The 2D and 1D probes are mounted with certain angles; α_{2D} is approximately equal to α_{1D}. The specific values result from a precise optical alignment. The two probes are mounted on a high precision traverse system which can be moved in wall-normal z direction in steps of $\Delta z = 0.01$ mm. By moving the probes up and down, the velocity can be measured at various distances from the wall. We defined the lower surface of the glass plate as the position $z = 0$ mm. It grows with increasing distance from the plate. In order to determine this position in our experiment the near-wall domain of the measured mean velocity profile has been extrapolated by a linear function, and the intersection point with zero velocity has been set to $z = 0$ mm.

First, the measurement of the velocity profiles was performed with a focal length of the probes of 160 mm. In this configuration the size of the measurement volume, the region where the laser beams interfere, amounts to $l_{mv_x} = 75$ μm, $d_{mv_z} = 200$ μm. This is 50 times smaller than the typical thickness of the viscous BL in our experiment. The angle between the optical axes in this configuration was $\alpha_{1D} = \alpha_{2D} = 24.5^\circ$. The measuring depth of the profile is confined by the frame size ($\phi = 95$ mm) of the observation window, which is embedded in the cooling plate. As a consequence, an additional measurement with a longer focal length of 500 mm is necessary to measure the whole profile up to a distance of 180 mm. The angle in this configuration was $\alpha_{1D} = \alpha_{2D} = 6.5^\circ$. To guarantee a sufficiently high number of statistically independent measurements, the experiment time for each position was set to 1 hr. Cold-atomized droplets of Di-Ethyl-Hexyl-Sebacat (DEHS) with a size of about 1 μm have been injected through an opening in the convection cell. They serve as tracers for the LDA measurement, and they are basically free of inertia. The particles have been added at least 1 min before we start a new measurement to give the flow sufficient time to mix them.

The LDA burst signal rate depends on the concentration of the DEHS particles and the distance to the wall. It varies between 1 and 200 Hz. In order to obtain reliable data free of statistical errors it is required to have a relatively high burst signal rate of each channel even at the position where the velocity is almost zero. Therefore the "noncoincidence" burst mode was used. When a seeding DEHS particle is passing through the outskirts of the measuring volume it generates a velocity sample burst on all channels simultaneously. This is denoted the "coincidence" burst mode, otherwise it is denoted "noncoincidence" burst mode. After the acquisition of the data a three-step process is required to obtain the Cartesian velocity components u, v, and w. It includes the following:

(1) Detection and elimination of obvious outliers

(2) Resampling of the "skewed" time series $u_1(t)$, $u_2(t)$, $u_3(t)$ to make them equidistant

(3) Transformation into Cartesian components $u(t)$, $v(t)$, and $w(t)$.

In the first step obvious outliers were detected and eliminated. One of the reasons for the outliers is the scattering of the laser light at the glass window. This happens mostly when measurements are conducted in the vicinity of the cooling plate. As the distance to the plate increases the number of outliers decreases significantly. The outliers have to be removed since they may cause statistical errors. A moving average G_i has been calculated for a window of 20 measured values:

$$G_i = \frac{1}{20} \sum_{j=i-10}^{i+9} \overline{x}_j \quad \text{for} \quad i > 10\,. \tag{1}$$

The bounds have been set according to three times the standard deviation of this interval:

$$\sigma_i = \sqrt{\frac{1}{20} \sum_{j=i-10}^{i+9} (x_j - G_i)^2} \quad \text{for} \quad i > 10\,. \tag{2}$$

All samples outside this band have been removed from the time series. It should be noted here that the number of outliers turns out to be only a very small fraction of the total number of samples within every time series. Thus, the elimination of these values is justified.

The second step is the interpolation and the resampling of the nonequidistant data to make it equidistant. We have tested three different sampling rates $f_s = 25$, 50, and 75 Hz, and we found that at $f_s = 50$ Hz the Fourier spectrum shows a sufficiently small but well-pronounced plateau. Four different interpolation methods have been investigated: interpolation of the nearest neighbors, linear interpolation, cubic Hermite interpolation, and cubic spline interpolation. The first interpolation method was not further used since the trend between the measured values is ignored. The linear and cubic Hermite interpolation resulted in smoother and closer interpolated curves than the cubic spline interpolation when compared with the original sample. The Hermite interpolation was eventually taken.

In the third step the velocity components u, v, and w are calculated according to the following transformation matrix:

$$\begin{pmatrix} u \\ v \\ w \end{pmatrix} = \begin{pmatrix} 1 & 0 & 0 \\ 0 & -\frac{\sin\alpha_2}{\sin(\alpha_1-\alpha_2)} & \frac{\sin\alpha_1}{\sin(\alpha_1-\alpha_2)} \\ 0 & \frac{\cos\alpha_2}{\cos(\alpha_1-\alpha_2)} & -\frac{\cos\alpha_1}{\cos(\alpha_1-\alpha_2)} \end{pmatrix} \begin{pmatrix} u_1 \\ u_2 \\ u_3 \end{pmatrix}. \tag{3}$$

This angular transformation matrix is used in correspondence with the software user guide manual of the LDA equipment [17]. In the measurement we measured three random components "u_1, u_2, and u_3"; our desired components "u, v, and w" were corrected by this matrix afterwards. In Fig. 1, measurement setup and coordinate system are shown. With the measurement arrangement, one of the horizontal velocity components u_1 is measured directly. The angles were measured with an uncertainty of 0.5°, which is sufficient for the present measurement setups.

Regarding the wall-normal velocity component, we met some technical difficulties during the measurement. From the transformation matrix, the wall-normal velocity component w is calculated as the weighted difference of u_2 and u_3. In this case it is very important that the two probes should be vertically very well aligned. If this is not the case, an "increasing" wall-normal velocity results, which is caused rather by the adjustment error than by the flow. Therefore a careful LDA calibration by a laser beam diagnostic system is necessary. Coherent LaserCam-HR and the height difference

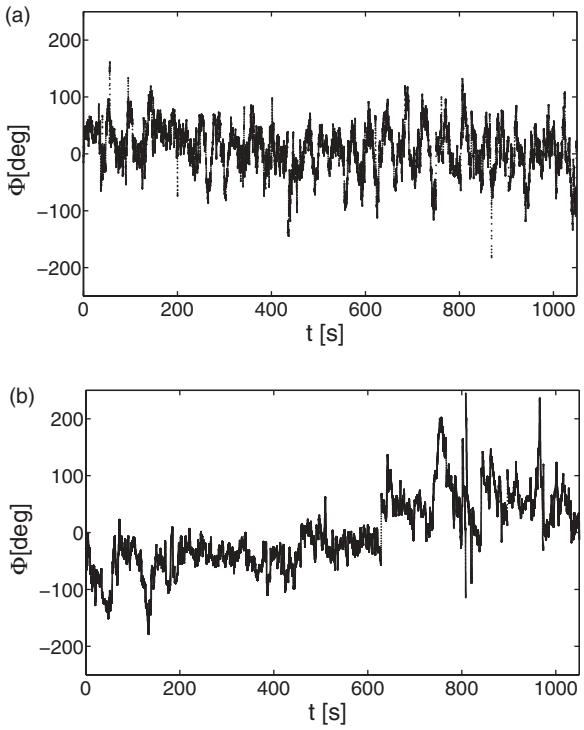

FIG. 2. Orientation of the horizontal velocity vector. (a) Experiment and (b) DNS data are taken at the center line. Times from the DNS have been recalculated to the experimental ones.

can be limited within 0.1 mm. Note also that the error of the wall-normal velocity is proportional to the longitudinal size of the measuring volume. One way to avoid these biases is to measure the wall-normal velocity component by the shorter focal length lens. The increased angle between the probes α gives then a five times smaller weighting factor for w. Furthermore, the smaller measuring volume can be guided closer the cooling plate.

Due to the arbitrary and fluctuating orientation of the LSC in the cylindrical cell (see, e.g., Resagk *et al.* [18]), we study the magnitude of the horizontal velocity

$$U = \sqrt{u^2 + v^2}\,, \tag{4}$$

instead of one of the single velocity components, u or v. In Fig. 2 time series of the instantaneous angle of the horizontal velocity vector at the center line are plotted. While the orientation of the velocity vector (and thus that of the LSC) seems to be locked in the experiment due to small imperfections of the RB cell [see Fig. 2(a)], the oscillation of the vector drifts slowly in the DNS [see Fig. 2(b)].

B. Temperature measurement

The temperature was measured by a small, glass-encapsulated microthermistor of a size of 125 μm. It should be noted that the typical thickness of the boundary layers is of the order of 10 mm at the Rayleigh numbers covered in this work. The size of the sensor is thus very small compared with the typical BL thickness. All measurements were performed at the corresponding positions where the velocity measurements have been done. Each single measurement covers the distance between $z = 70$ μm (corresponding half of the diameter of the microthermistor) and $z = 150$ mm. The thermistor is connected to the tips of two 0.3 mm supports by 18 μm wires. In order to reduce the measurement error we have redesigned the temperature sensor taking care that the connecting wires were aligned parallel to the plates and along the isosurfaces of constant mean temperature in the flow. Furthermore, the sensor has been calibrated in a calibration chamber using a Resistance Temperature Detector (RTD) of PT 100 type certified by the Deutsche Kalibrierdienst as reference. The measurement uncertainty of the RTD is specified with 0.02 K in the range between 0° and 100°. The microthermistor is connected to a special resistance bridge with an internal amplifier providing a very low current of $I_{\mathrm{Th}} = 5$ μA sufficiently small to keep the self-heating of the sensor as low as 10 mK. The bridge was connected to a PC-based multichannel data acquisition system with a resolution of 10^{-4} K and a sampling rate of 200 s^{-1}.

III. DIRECT NUMERICAL SIMULATION

In the direct numerical simulations the three-dimensional Boussinesq equations are solved, which are given by

$$\frac{\partial \vec{u}}{\partial t} + (\vec{u}\cdot\boldsymbol{\nabla})\vec{u} = -\frac{1}{\rho_0}\boldsymbol{\nabla} p + \nu\nabla^2\vec{u} + g\alpha T\vec{e}_z, \tag{5}$$

$$\frac{\partial T}{\partial t} + (\vec{u}\cdot\boldsymbol{\nabla})T = \kappa\nabla^2 T, \tag{6}$$

$$\boldsymbol{\nabla}\cdot\vec{u} = 0\,. \tag{7}$$

Here $\vec{u} = (u,v,w)$ is the velocity field, p is the pressure field, and T the temperature field. The characteristic velocity is the free-fall velocity $U_f = \sqrt{g\alpha\Delta\vartheta H}$. The characteristic time is the free-fall time $T_f = H/U_f$. Owing to the cylindrical geometry we switch from Cartesian to cylindrical coordinates, (x,y,z) to (r,φ,z). Boundary conditions are the no-slip condition for the velocity at all walls, isothermal top and bottom plates, and adiabatic side walls for the temperature. The grid sizes are $N_r \times N_\varphi \times N_z = 301 \times 513 \times 360$ for the smaller Ra and $513 \times 1153 \times 861$ for the larger one. We use the DNS scheme by Verzicco and Orlandi in which the equations are solved on a staggered grid with a second-order finite difference scheme [19,20]. The pressure field p is determined by a two-dimensional Poisson solver after applying a one-dimensional fast Fourier transform in the azimuthal direction. The time advancement is done by a third-order Runge-Kutta scheme. The grid spacings are nonequidistant in the axial and radial directions. The grid resolutions are chosen sufficiently large (see Ref. [21] for more details). The thermal BL is resolved with 18 grid planes for $\mathrm{Ra} = 3 \times 10^9$ and with 35 grid planes for $\mathrm{Ra} = 3 \times 10^{10}$.

In order to compare the results with the experiments in BOI we follow their measurement procedure and take time series of the turbulent fields at several locations in the cell, which allow us to determine wall-normal mean profiles of the turbulent fields. For the lower Ra there are four arrays containing 40 measurement points each. They have been seeded in order to track fully resolved time series of the three velocity components and the temperature. The probe array center is located in the center line. Probe arrays 1, 2, and 3 are arranged at $r = 0.88$ R and $\varphi = 0$, π and $3\pi/2$ as can be seen

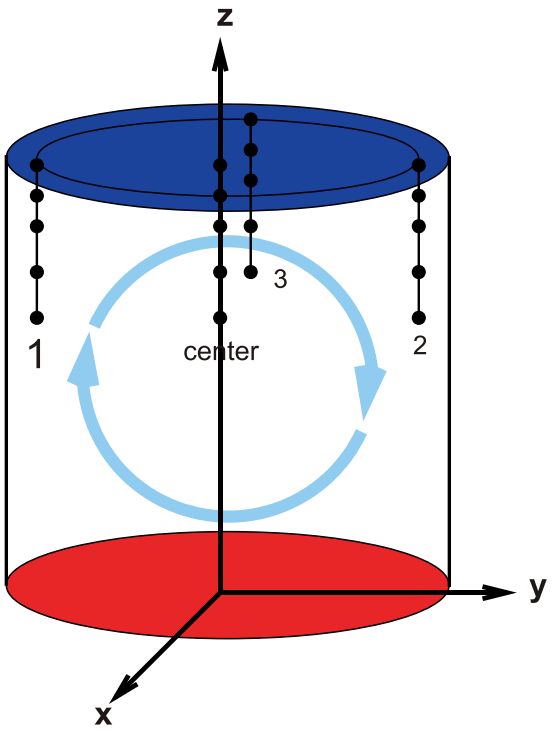

FIG. 3. (Color online) Sketch of the arrays with the measurement locations. Probe array entitled center is located at the center line $(r, \varphi) = (0, 0)$, array 1 at (0.88 R, 0), array 2 at (0.88 R, π), and array 3 at (0.88 R, $3\pi/2$).

in Fig. 3. This setup is designed in correspondence with the arrangement in the BOI. There are 100 measurement points for larger Ra run.

IV. RESULTS

A. Velocity profiles at center line

We present first the mean velocity profiles at $\mathrm{Ra} = 3 \times 10^9$ and 3×10^{10} and start with the comparison of the mean horizontal velocity profiles at the center line, $\langle U(z) \rangle$, as shown in Fig. 4. The symbol $\langle \cdot \rangle$ stands for an average over the time series taken in the studies, and U is defined by Eq. (4). The experimental mean velocity profiles at $\mathrm{Ra} = 3 \times 10^9$ and 3×10^{10} are plotted as closed circles, and the corresponding DNS results as open circles. They are normalized by the maximum mean velocity. Additionally the Blasius solution of the two-dimensional BL equations [9] is plotted. The data show that the measured and numerical mean velocity profiles agree well for both Rayleigh numbers. In the case of $\mathrm{Ra} = 3 \times 10^9$, both mean velocity profiles show a linearly increasing fraction of the profile; they have a maximum difference of 9% at a height that corresponds with BL thickness.

Additionally, we can address the question whether the profiles of the mean velocity of turbulent RB convection match with the laminar Prandtl-Blasius prediction [9]. It has been already found in a previous study by du Puits *et al.* [22] that the Blasius profile does not provide a good approximation to the measured profiles of the mean horizontal velocity in turbulent RB convection. These measurements covered a range of Rayleigh numbers of one order of magnitude around $\mathrm{Ra} = 10^{11}$. In the present work we can extend this range and show results at lower Rayleigh numbers of $\mathrm{Ra} = 3 \times 10^9$ and 3×10^{10}. In both cases, the near-wall part of the profiles grows almost linearly and coincides with the Prandtl-Blasius solution as visible in the inset of Fig. 4(a) and 4(b). Following their shape toward larger distances, the profiles noticeably start to deviate from the theoretical prediction of the laminar shear layer, especially for the velocity at the lower Ra. We can thus conclude that the Blasius profile cannot perfectly describe the profiles of the mean velocity in turbulent RB convection for the range of Rayleigh numbers which is accessible in the measurements and simulations. The dynamic rescaling which has been suggested in Ref. [12] has been discussed in Ref. [21] for the DNS. It cannot be performed in the measurements since the time series for the profiles are taken point by point. The interesting phenomenon is that all the horizontal velocity profiles are systematically smaller than Prandtl-Blasius prediction, within the investigated Ra numbers between $\mathrm{Ra} = 10^9$ and 10^{12}. A reason might be the extraction of kinetic energy from the horizontal motion in order to supply the wall-normal disturbances.

The standard deviation (or root-mean-square) of the horizontal velocity, $\sigma_U(z)$ is shown in Fig. 4(c) and 4(d). The profiles are normalized by their maximum values respectively. The comparison of the data at $\mathrm{Ra} = 3 \times 10^9$ and 3×10^{10} indicates a very good agreement except for a sudden drop (see also Ref. [14] for a detailed discussion) in the measured profile at $\mathrm{Ra} = 3 \times 10^{10}$. The local maximum of the profile is for both places at about the same distance from the wall although the BL gets thinner. Again the agreement seems to improve slightly for the larger Rayleigh numbers.

The mean profiles of the wall-normal velocity component, $\langle w(z) \rangle$, are plotted in Fig. 5(a) and 5(b). The good agreement between the measured data and the DNS data gives us the information that at $\mathrm{Ra} = 3 \times 10^9$ and 3×10^{10}, the mean wall-normal velocities tend to zero, namely, there is no mean vertical velocity. Our result is in agreement with the PIV measurements by Sun *et al.* [11]. Note that this is, however, in contrast to the classical Prandtl-Blasius solutions for an incompressible fluid, which obey a vertical velocity profile due to the displacement effect of the BL. The jump of the data is the place where we switched from the short to the long focal length lens. Due to the specific arrangement of the LDA probes the wall-normal velocity component is extremely sensitive to small misalignments. The change in the lenses requires a complete readjustment of the probes, and the result shown in the plot is actually the best one that we can achieve. Nevertheless, the profile shows a clear trend of a zero mean wall-normal velocity, which is consistent with a 3D flow structure in an incompressible flow setting. As we can also see, the wall-normal standard deviations, $\sigma_w(z)$, are not zero right above the wall. This can be seen from the data compared in Fig. 5(c) and 5(d). The fluctuations keep increasing to magnitudes that are comparable to the horizontal components. The bump of the experimental data at $z/h < 10^{-3}$ is the error caused by the scattering light reflected by the glass window surface. This problem is inevitable for all LDA measurements very close to a solid surface. The profiles of the root mean square (rms) of the vertical

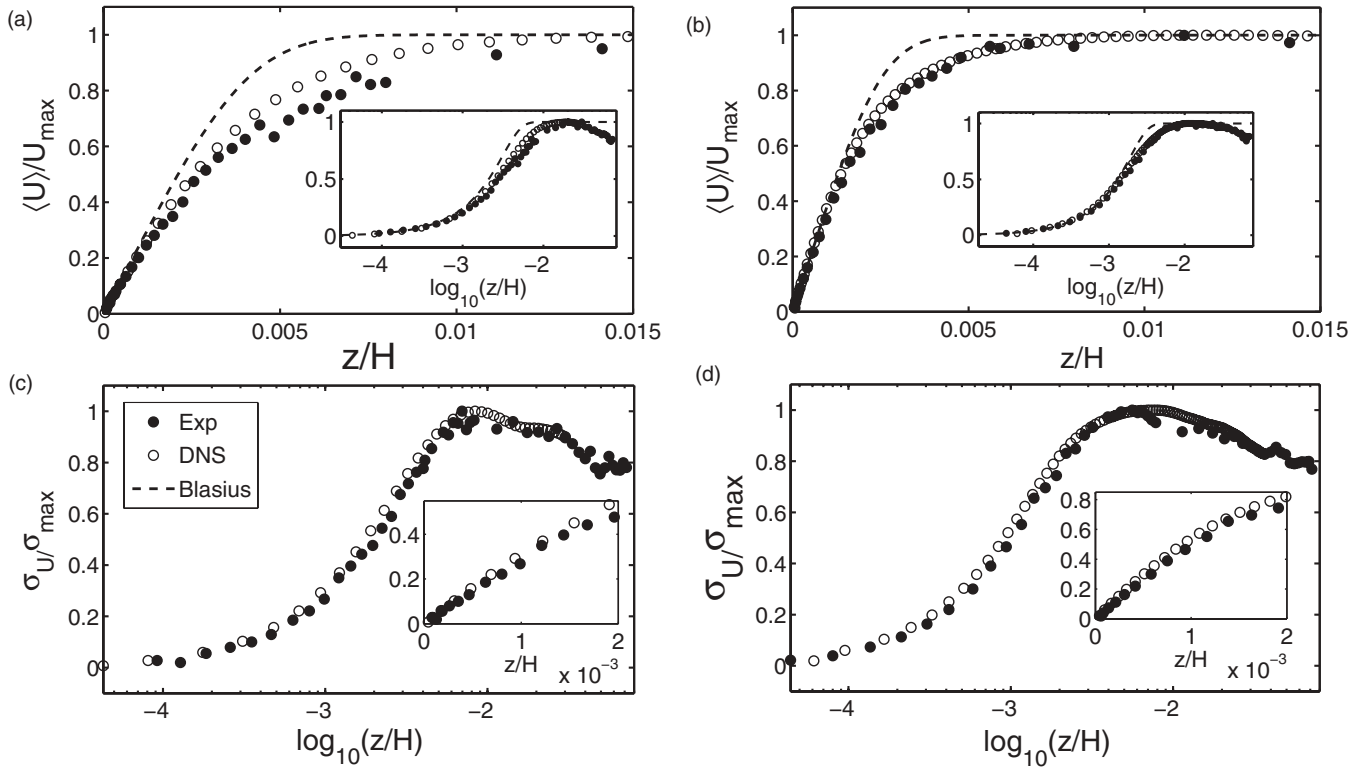

FIG. 4. Profiles of the mean horizontal velocity (a,b) and the standard deviation (c,d) measured in the experiment (closed circles) and obtained from the DNS (open circles) at $\mathrm{Ra} = 3 \times 10^9$ (a,c) and $\mathrm{Ra} = 3 \times 10^{10}$ (b,d). The dashed lines in (a) and (b) represent the velocity field of a laminar flat plate BL according to Blasius [9]. The insets of (a) and (b) show the entire mean velocity profile in logarithm scale, and the insets of (c) and (d) show the near-wall region of the BL fluctuations.

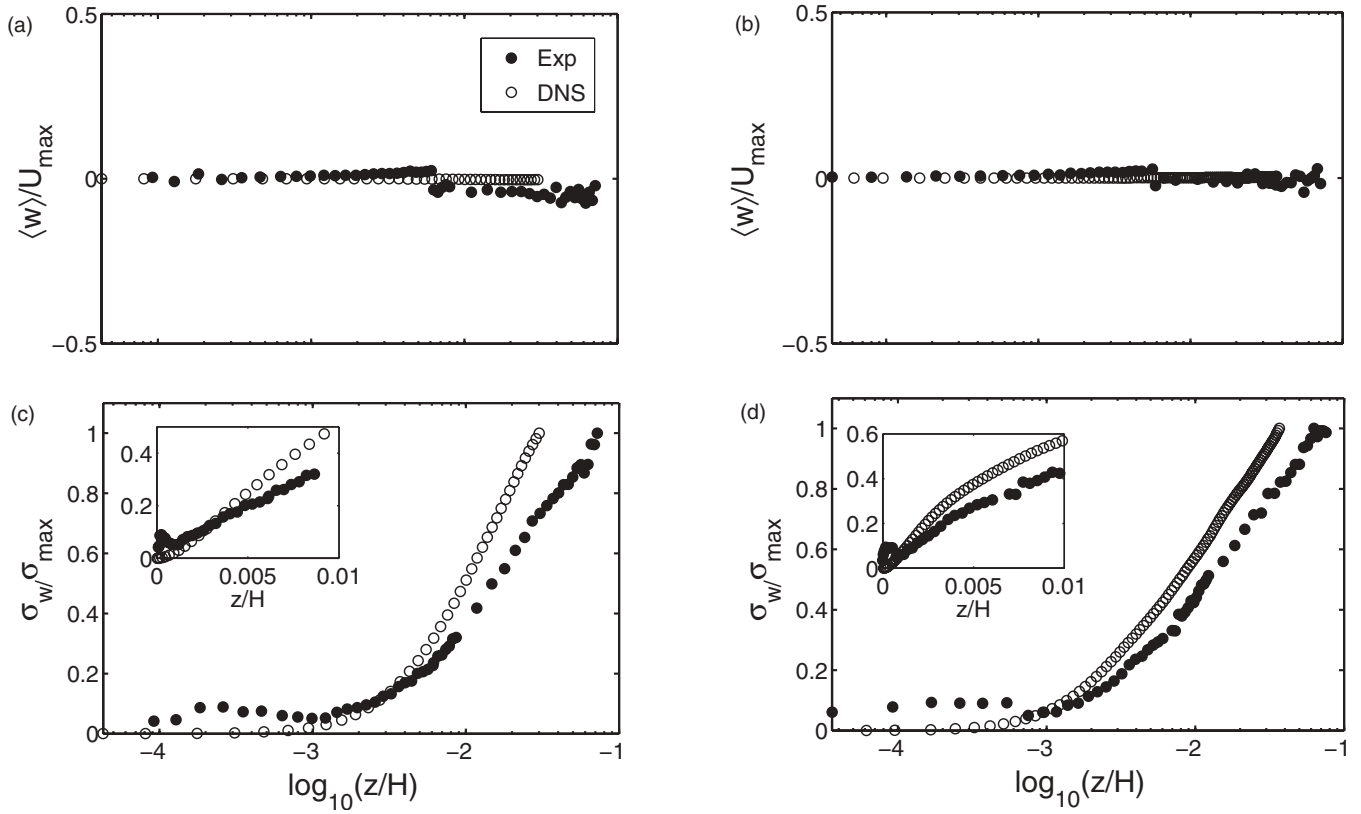

FIG. 5. Profiles of the wall-normal velocity (a,b) and the standard deviation (c,d) measured in the experiment (closed circles) and obtained from the DNS (open circles) at $\mathrm{Ra} = 3 \times 10^9$ (a,c) and $\mathrm{Ra} = 3 \times 10^{10}$ (b,d). The insets show the near-wall region of the BL.

component in the experiment and DNS fit well to being zero at both Rayleigh numbers in the region $0 < z/H < 10^{-3}$, i.e., well within BL. For $z/H > 10^{-3}$ the rms value $\sigma_w(z)$ is strongly increasing. For completeness, the measured viscous BL thicknesses are $\delta_{v,d}/H = 3.8 \times 10^{-3}$ for $\mathrm{Ra} = 3 \times 10^9$ and $\delta_{v,d}/H = 1.7 \times 10^{-3}$ for $\mathrm{Ra} = 3 \times 10^{10}$. This implies that the fluctuations of the vertical velocity component start to increase rapidly at the edge of the BL. The viscous BL thickness $\delta_{v,d}$ is here calculated by the displacement method, which will be discussed below.

B. Temperature profiles at center line

Having discussed the mean profiles of the velocity components so far, we now turn to the mean temperature profiles, $\langle T(z)\rangle$, which are displayed in Figs. 6(a) and 6(b). The mean temperature profiles are normalized by the temperature difference as measured between the bulk and cooling plate. The agreement between the measurement and the numerical data is not as perfect as for the velocity data but still satisfactorily good. A very detailed view close to the plate surface, however, shows that the measured mean temperature gradients at the wall $d\langle T(z)\rangle/dz|_{z=0}$ strongly differ from the DNS data. It exceeds the value from the DNS by a factor of 2.5 at $\mathrm{Ra} = 3 \times 10^9$ and by a factor of 1.5 at $\mathrm{Ra} = 3 \times 10^{10}$. In other words, the local heat flux in the experiment is 2.5 (1.5) times larger than the numerical one. Currently we do not have a conclusive explanation for this difference. We can state here only that measurements and DNS have been performed with the highest possible diligence and the results are verified in multiple ways. We are also aware about this difference with other RB convection measurements [23,24] and other very recent DNS results [12,25]. However, we believe that our measurements are well verified for the following reasons [26]:

(1) Each sensor has passed a complex calibration process resulting in an accuracy of better than ± 10 mK.

(2) In addition to the profile measurement with the microthermistor the plate temperature at the cell center and the temperature in the bulk have been measured with two independent temperature probes. The measured values coincide very well.

(3) The size of the sensor is very small compared with the typical boundary layer thickness and amounts only to about 1/100 of the one.

(4) The plate surface within a radius of 0.5 m around the measurement position is smooth. The roughness amounts to less than 5 μm corresponding 0.05% of the minimal boundary layer thickness.

We have also investigated if the Pohlhausen prediction [27] for the temperature profile fits with our results. The Pohlhausen solution builds on the Blasius solution for the laminar BL and assumes that the temperature is passively advected in the flow. We found that both the experimental and numerical mean profiles, deviate from this prediction. In Ref. [21] it is demonstrated that one reason for these deviations are the permanent detachments of fragments of the thermal BL into the bulk, the so-called thermal plumes. The standard deviation of the temperature, $\sigma_T(z)$, is plotted Figs. 6(c) and 6(d). They

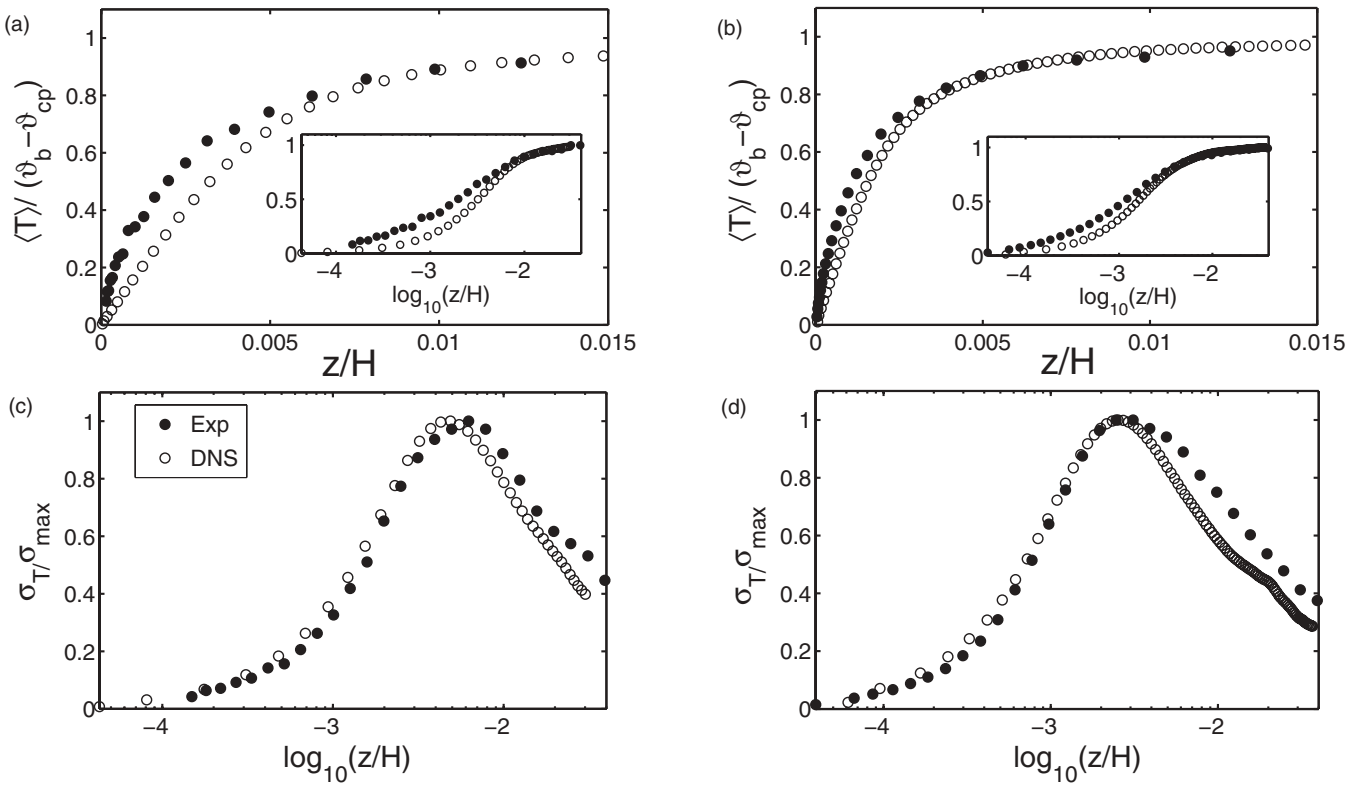

FIG. 6. Profiles of the mean temperature (a,b) and the standard deviation (c,d) measured in the experiment (closed circles) and obtained from the DNS (open circles) at $\mathrm{Ra} = 3 \times 10^9$ (a,c) and $\mathrm{Ra} = 3 \times 10^{10}$ (b,d). The insets show the entire mean temperature profile in logarithm scale. Here ϑ_b and ϑ_{cp} denote the mean bulk temperature and the surface temperature of the cooling plate.

are normalized by maximum amplitude. It can be seen that they have the same trend in both panels. At Ra $= 3 \times 10^9$, the temperature fluctuations have 10%–20% difference from each other before they approaching their maximum fluctuation, for larger distances away from the wall the difference gets smaller to about 5%. At Ra $= 3 \times 10^{10}$, the fluctuations agree quite well, especially up to the maximum fluctuation. For larger z, we find a difference by about 10% in comparison to the DNS.

C. Boundary layer scaling

1. Viscous and thermal boundary layer thicknesses

We now turn to the scaling analysis of the local BL thickness with respect to the Rayleigh number. We compute the displacement thicknesses for the horizontal velocity U and the temperature T according to the following definitions [28]:

$$\delta_{v,d} = \int_0^\infty \left[1 - \frac{\langle U(z)\rangle}{U_{\max}}\right] dz, \tag{8}$$

$$\delta_{\theta,d} = \int_0^\infty \left[1 - \frac{\langle T(z)\rangle - \vartheta_{cp}}{\vartheta_b - \vartheta_{cp}}\right] dz, \tag{9}$$

where ϑ_b and ϑ_{cp} are the mean temperature in the bulk and the fixed temperature at the surface of the cooling plate. The displacement thickness is one of the possible measures of the boundary layer thickness. It is defined as the distance by which the surface has to be displaced to compensate the reduction in flow rate due to the effect of the boundary layer. We compute the integrals numerically by a trapezoidal rule. In Fig. 7 we summarize the obtained BL thickness values versus the corresponding Rayleigh numbers in a range between Ra$= 10^9$ to 10^{12}. The data points at Ra $= 3 \times 10^9$ and 3×10^{10} are from the present work, and the data points at the higher Ra numbers are from our previous work [22]. The plots are given in double logarithmic axes such that a possible algebraic scaling becomes visible right away. The viscous and thermal BL thicknesses are normalized by the constant height of the cylindrical cell $H = 2.55$ m.

The measured values of both BL thicknesses, the viscous and the thermal one, agree perfectly with the data from the DNS. Adding the experimental data from the previous work both quantities scale with Ra as well as with Re_g according to power laws $\delta_{v,d}/H = C_{1,d}\mathrm{Ra}^\beta$, $\delta_{\theta,d}/H = C_{2,d}\mathrm{Ra}^\gamma$, $\delta_{v,d}/H = C_3\mathrm{Re}_g^\epsilon$, and $\delta_{\theta,d}/H = C_4\mathrm{Re}_g^\eta$; the prefactors and the exponents have been computed as $C_{1,d} = 0.66 \pm 0.51$, $C_{2,d} = 0.76 \pm 0.33$, $C_3 = 0.64 \pm 0.66$, $C_4 = 0.54 \pm 0.13$, $\beta = -0.24 \pm 0.03$, $\gamma = -0.24 \pm 0.02$, $\epsilon = -0.54 \pm 0.09$, and $\eta = -0.51 \pm 0.02$. The obtained exponent β is quite different from those of previous experiments, $\beta = -0.16$, made in water [29]. Recall, however, that the BL thickness of experiment with water is only about 1 mm and thus poses much higher requirements on the resolution. We conclude that the discrepancy is mostly due to different aspect ratios and Pr numbers. It should also be noted that our scaling laws describe the behavior of the local BL thickness at the central axis of the cylindrical cell and must not necessarily agree with the prediction of the global scaling. Nevertheless, β perfectly fits the prediction of the global exponent according to the phenomenological scaling theory of Grossmann and Lohse [7]. The exponent γ is slightly lower than expected from the global

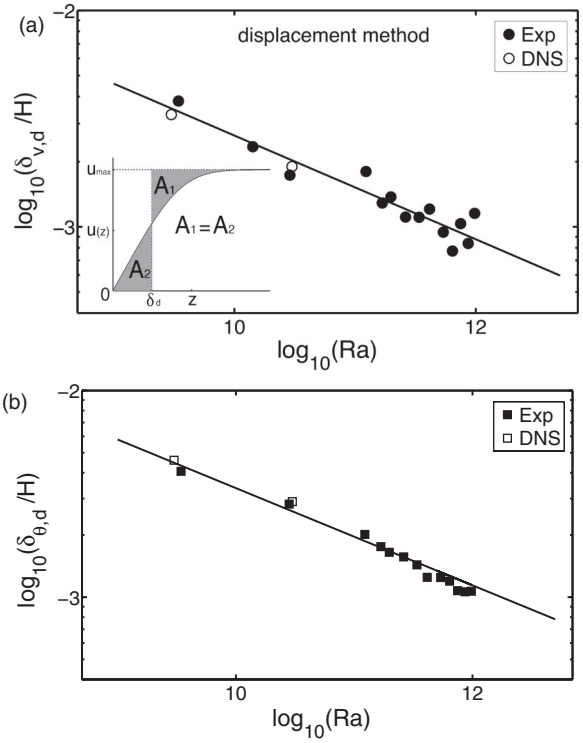

FIG. 7. Displacement thickness of the viscous (a) and thermal (b) boundary layers versus Ra. Experimental results are displayed as closed symbols, DNS data points are open symbols. The solid lines in each of the graphs correspond to power laws $\delta_{v,d}/H = 0.66\ \mathrm{Ra}^{-0.24}$ and $\delta_{\theta,d}/H = 0.76\ \mathrm{Ra}^{-0.24}$, respectively.

scaling $\mathrm{Nu} \sim \mathrm{Ra}^{\gamma''}$, and the exponent ϵ is slightly higher than from $\delta_v = 0.25L\mathrm{Re}^{-0.5}$. Moreover it should be mentioned that both the viscous and the thermal boundary layers exhibit approximately the same thickness, which is consistent with the Prandtl number of about unity.

It is useful to complement the analysis of the BL scaling by the slope method [30] for the computation of the BL thickness. The latter is more widely used in the RB convection flow. The principles of both displacement and slope methods are sketched in the insets of Fig. 7(a) and Fig. 8(a). Although this method is very popular in the RB community, the results are more uncertain than for the displacement thickness. The slope method is based on the near-wall gradient of the velocity and the temperature profile. First, we extrapolate the linear part of the velocity profile; then we get the viscous BL thickness from the intersection value of the extrapolation and the first local maximum of the mean velocity. For the thermal BL thickness, we fit the mean temperature profile in the range of $0 < z < 2.07$ mm by the function $y = ax^2 + bx + c$, then compute the thermal BL thickness by the gradient, namely, $\delta_{\theta,s} = 1/b$. According to power laws $\delta_{v,s}/H = C_{1,s}\mathrm{Ra}^{\beta'}$, $\delta_{\theta,s}/H = C_{2,s}\mathrm{Ra}^{\gamma'}$; the prefactors and the exponents are $C_{1,s} = 0.90 \pm 1.22$, $C_{2,d} = 0.42 \pm 0.09$, $\beta' = -0.24 \pm 0.03$, $\gamma' = -0.24 \pm 0.01$. The slope method does not change the BL scaling exponent compared to the displacement method. In the case of the thermal BL, it unravels the differences between the DNS and the experiment, which have been discussed already in Sec. IV. The conclusion is that we have the same

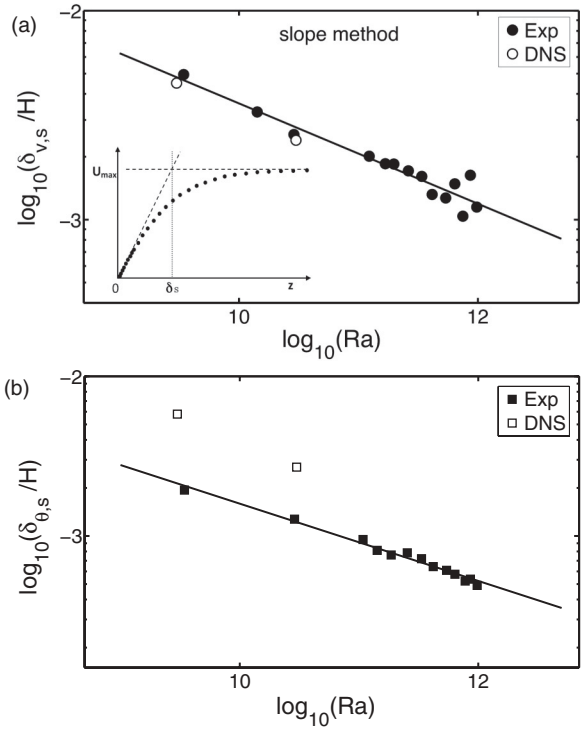

FIG. 8. Thickness of the viscous (a) and thermal (b) boundary layers versus Ra according to the slope method. Experimental results are displayed as closed symbols, DNS data points are open symbols. The solid lines in each of the graphs correspond to power laws $\delta_{v,s}/H = 0.90\ \mathrm{Ra}^{-0.24}$ and $\delta_{\theta,s}/H = 0.42\ \mathrm{Ra}^{-0.24}$, respectively.

exponents of scaling laws even by the slope method, though the BL thicknesses calculated by this method are thinner than computed by displacement method.

2. Shear Reynolds number

The shear Reynolds number has been defined as a criterion to judge about the potential transition of a BL from the laminar toward the turbulent state [31]. It is given by

$$Re_s = \frac{\delta_v U}{\nu}, \tag{10}$$

where δ_v is the viscous BL thickness, U is a typical velocity of the outer velocity BLs, and ν is the kinematic viscosity. For an isothermal, zero-pressure BL according to the model of Prandtl and Blasius, the authors in Ref. [31] estimated a critical value of $\mathrm{Re_s} \approx 420$. In turbulent RB convection the stability of the BL may not only be disturbed by the shear which increases with rising velocity but also by thermal plumes detaching from the BL or by coherent structures in the flow field. These effects may lower the stability limit of the BL and may induce a transition towards a turbulent regime even at significantly smaller $\mathrm{Re_s}$ (e.g., Preston predicted $\mathrm{Re_s} = 320$, based on momentum boundary layer thickness [32]). In Fig. 9 we plot shear Reynolds numbers in a range between $\mathrm{Ra} = 10^9$ and 10^{12}. $\mathrm{Re_s}$ keeps increasing with Ra, and, again, experimental and numerical data fit very well. In order to estimate the Ra numbers at which the trend crosses the critical limits $\mathrm{Re_s} = 320$ or $\mathrm{Re_s} \approx 420$ we extrapolated the data points using a regression $\mathrm{Re_s} \sim \mathrm{Ra}^{0.267\pm0.0386}$. According to this fit the lowest possible Ra number for a transition to a turbulent state amounts to $\mathrm{Ra_c} \approx 2 \times 10^{12}$, which would be below the prediction of Grossmann and Lohse in Ref. [7] and the recent experimental findings by Funfschilling *et al.* [33]. However, it cannot be ruled out that due to the plume inside the BLs as well as the strongly three-dimensional flow in turbulent RB convection and the complex dynamics of the LSC this transition may take place at even lower Rayleigh numbers. The exact parameters and the results can be found in Tables I and II.

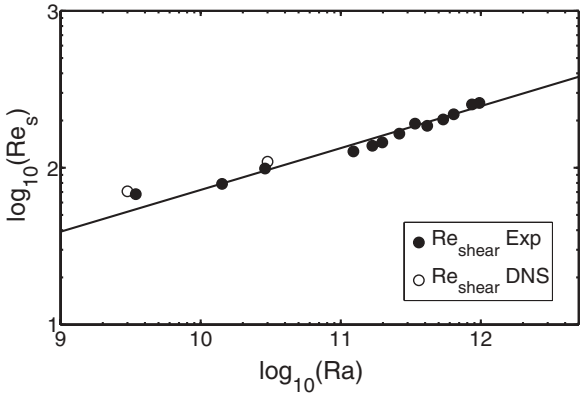

FIG. 9. Shear Reynolds number $\mathrm{Re_s}$ versus Ra from experiment (closed circles) and DNS (open circles). The solid line is the fit to all data.

D. Boundary layer out of center

In RB cells of aspect ratio one and smaller the sidewall significantly affect the flow inside the cylindrical enclosure. Therefore, it is justified to ask whether or not the results obtained at the center of the cooling plate can be generalized to the entire area. We will discuss measurements and numerical

TABLE I. Set of parameters and selected results of the velocity measurements ($\Gamma = 1, \mathrm{Pr} = 0.7$). Ra is the Rayleigh number adjusted during the measurements, respectively, $\bar{v}_{\max}$ is the maximum of the velocity, Re_s is shear Reynolds number, Re_g is global Reynolds number, $\delta_{v,d}$ and dimensionless $\delta_{v,d}/H$ are the displacement thicknesses for the viscous boundary layer.

Ra	$\bar{v}_{\max}$ (m/s)	Re_s	Re_g	$\delta_{v,d}$ (mm)	$\delta_{v,d}/H$
3.44×10^9	0.097	68	1.49×10^4	9.532	0.00381
1.42×10^{10}	0.168	79	2.57×10^4	5.863	0.00235
2.88×10^{10}	0.224	99	3.41×10^4	4.335	0.00173
1.23×10^{11}	0.179	133	7.36×10^4	11.35	0.00180
1.68×10^{11}	0.212	112	8.71×10^4	8.12	0.00129
1.98×10^{11}	0.220	124	9.00×10^4	8.66	0.00137
2.62×10^{11}	0.262	118	1.06×10^5	6.99	0.00111
3.39×10^{11}	0.301	134	1.21×10^5	6.97	0.00111
4.14×10^{11}	0.339	162	1.34×10^5	7.61	0.00121
5.38×10^{11}	0.404	149	1.57×10^5	5.95	0.00094
6.40×10^{11}	0.435	129	1.67×10^5	4.87	0.00078
7.48×10^{11}	0.503	195	1.89×10^5	6.52	0.00103
8.64×10^{11}	0.545	167	2.00×10^5	5.28	0.00084
9.77×10^{11}	0.607	251	2.17×10^5	7.27	0.00115

TABLE II. Set of parameters and selected results of the temperature measurements ($\Gamma = 1$, $\mathrm{Pr} = 0.7$). Ra is the Rayleigh number adjusted during the measurements, respectively, Re_g is global Reynolds number, $\delta_{\theta,d}$ and dimensionless $\delta_{\theta,d}/H$ are the displacement thicknesses for the thermal boundary layer.

Ra	Re_g	$\delta_{\theta,d}$ (mm)	$\delta_{\theta,d}/H$
3.44×10^9	1.49×10^4	10.391	0.00416
2.88×10^{10}	3.41×10^4	7.211	0.00288
1.08×10^{11}	6.73×10^4	12.678	0.00201
1.42×10^{11}	7.77×10^4	11.063	0.00176
1.86×10^{11}	8.95×10^4	10.391	0.00165
2.54×10^{11}	1.05×10^5	9.875	0.00157
3.34×10^{11}	1.22×10^5	9.034	0.00143
4.19×10^{11}	1.37×10^5	7.857	0.00125
5.42×10^{11}	1.57×10^5	7.844	0.00125
6.37×10^{11}	1.71×10^5	7.532	0.00120
7.76×10^{11}	1.90×10^5	6.775	0.00108
8.59×10^{11}	2.00×10^5	6.955	0.00110
9.78×10^{11}	2.14×10^5	6.734	0.00107

results obtained at three other positions, 1, 2, and 3 (see Fig. 3). In our experiment with the small cell, we tried to lock the wind in a certain direction. We realized this by stretching the plexiglass sidewall along the diameter for about 1% on each side. Locking the wind in this way, we can assign certain positions at the plate to areas of upwelling and downwelling plumes (positions 1 and 2) as well as outside of the large-scale circulation (position 3). This assignment is not possible in the DNS since the mean angle of the LSC plane slowly drifts, and these distinct areas are not well defined (see Fig. 2). Because of the different behavior of the LSC we will, therefore, not directly compare the data from the experiment with the numerical ones in this section.

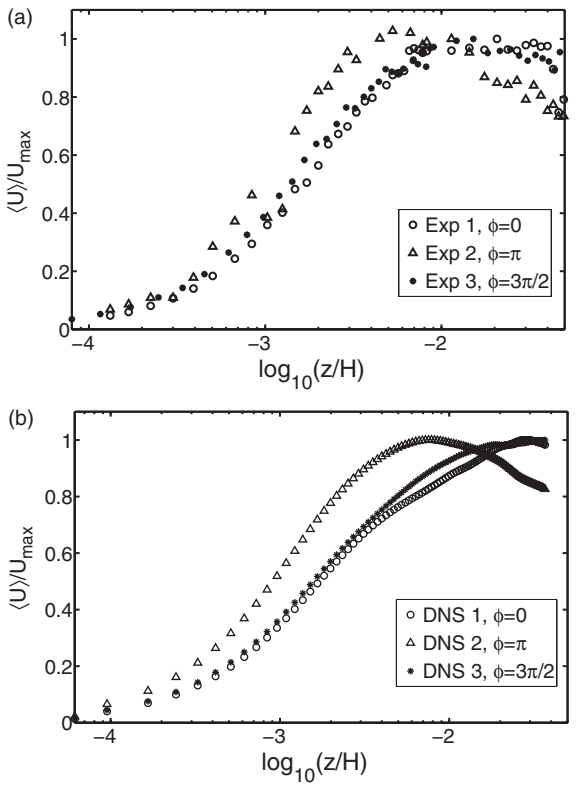

FIG. 10. Mean horizontal velocity profiles at side window 1, 2, and 3, which are located at $r = 0.88$ R and $\varphi = 0$, π, and $3\pi/2$; see Fig. 3. (a) Profiles of the measured data at $\mathrm{Ra} = 2.88 \times 10^{10}$, at window 1 (circle), window 2 (triangle), and window 3 (star). (b) Profiles of the DNS data at $\mathrm{Ra} = 3 \times 10^{10}$ at array 1 (circle), array 2 (triangle), and array 3 (star).

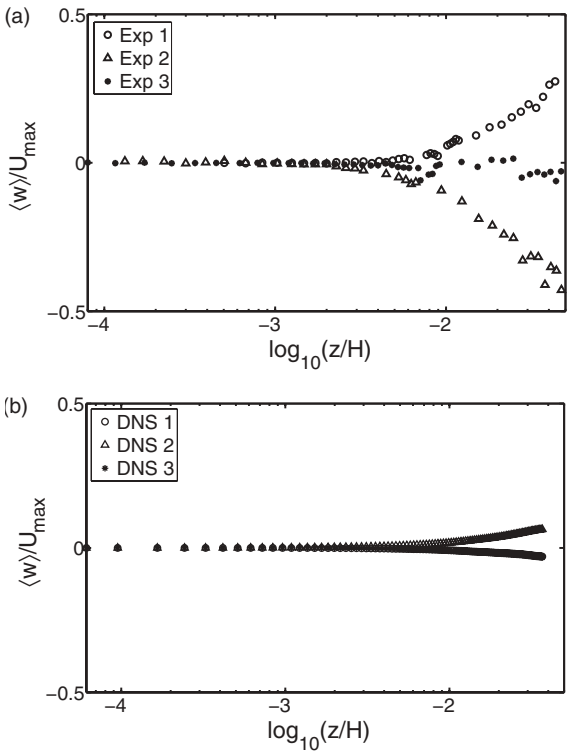

FIG. 11. Mean wall-normal velocity profiles at side window 1, 2, and 3. (a) Profiles of the measured data at $\mathrm{Ra} = 2.88 \times 10^{10}$, at window 1 (circle), window 2 (triangle), and window 3 (star). There is a clear pair of upwelling and downwelling mean velocities. (b) Profiles of the numerical data at $\mathrm{Ra} = 3 \times 10^{10}$ at array 1 (circle), array 2 (triangle), and array 3 (star).

First, we present the experimental and DNS mean horizontal velocity profiles at $\mathrm{Ra} = 3 \times 10^{10}$ in Fig. 10(a) and 10(b). In order to show a potential deviation from the profile at the central axis the velocity is normalized by the same value $U_{\max}$ as used in Figs. 4 and 5. The maximum of the velocity at the outer positions is significantly below the value at the center line. This implies a reduction of the local heat transfer coefficient and, hence, a decrease of the local Nu. In this work we do not quantify this effect, but it is certainly one topic that deserves closer attention in the future. All three measured profiles rise with a different gradient toward their maximum, and the thickness of the viscous BL varies. Unlike at the central axis of the experiment the mean wall-normal velocity at the windows 1 and 2 (begin and end of the path of the LSC along the cooling plate) clearly deviates from zero. At the area of upwelling plumes (1) a positive w component has been measured, while this velocity component is negative at the area of downwelling plumes. At window 3, which is

outside the LSC, the mean of w tends to zero. Since in the DNS areas of up- and downwelling plumes are not assigned with distinct positions at the cooling plate the observed effect is weaker, but clearly visible too [see Fig. 11(b)]. The viscous and thermal boundary layer thicknesses at these three locations have been calculated as well. Generally the thermal boundary layer thickness is always thicker than viscous boundary layer thickness, in our case at $\mathrm{Pr} = 0.7$. We found that boundary layer thickness is not uniform, and it is strongly dependent on its location. From the thinnest to the most thick boundary layers at all four locations we have measured, they have about a factor of 1.25 of their thicknesses.

V. CONCLUSIONS

The velocity and the temperature fields close to the horizontal plates in turbulent RB convection in air have been studied experimentally and numerically. At two Rayleigh numbers, $\mathrm{Ra} = 3 \times 10^9$ and 3×10^{10}, highly resolved measurements of all three velocity components and the temperature inside and outside the BL have been carried out. Localized high-resolution velocity and temperature results have been compared directly with data obtained from DNSs.

In summary, the measured velocity data agree very well with the DNS results, while the temperature data slightly differ. The mean horizontal velocity as well as the mean of the wall-normal component are in an excellent agreement. Both differ from the Blasius solution of a laminar nonisothermal shear layer. At the center line of the experiment the mean of the wall-normal velocity component holds at zero over a long range of the wall distance z. However, this component strongly fluctuates. Out of the center, particularly at the areas where the plumes hit or leave the horizontal plates a nonzero mean wall-normal velocity unequally from zero has been detected. We also found that the viscous BL thickness scales with the Ra as $\delta_v \sim \mathrm{Ra}^{-0.24}$, i.e., with the same exponent as predicted by Grossmann and Lohse [7]. In order to have a sufficiently long range in the Ra we added velocity data from previous experiments covering eventually Rayleigh numbers between $\mathrm{Ra} = 10^9$ and 10^{12}. We also discussed the shear Reynolds number and its trend with growing Ra since this quantity is one of the potential indicators of a transition towards a turbulent BL. Up to the highest Ra, $\mathrm{Ra} = 10^{12}$, it remains below the predicted transition limits $\mathrm{Re}_{s,c} = 320$ [32] or $\mathrm{Re}_{s,c} = 420$ [31]. Recall that both predictions have been made.

The measured mean temperature profiles slightly differ from the numerical results. In particular, the measured temperature gradients at the wall are significantly higher than those computed from the DNS. Furthermore, both measured profiles do not show the clear linear trend as seen in the DNS data. Even though the measurements have been carried out very carefully and the used microthermistor probes have been calibrated precisely, we do not have an explanation for these deviations. The local thickness of the thermal BL in the center line is found to scale with respect to the Ra as $\delta_\theta \sim \mathrm{Ra}^{-0.24}$, again slightly different from the global prediction in this range of Ra. The BL thickness is not constant; it depends on the different locations and time periods.

One task that had to remain open until now is the distribution of the heat flux into its diffusive and its convective fraction and how this ratio depends on the wall distance z. While the diffusive fraction can easily obtained from the gradient of the mean temperature a direct determination of the convective part requires simultaneous measurements of the wall-normal velocity component and the temperature at the same point. Recent DNSs by Wagner *et al.* show that the BL thickness of both the velocity and temperature field and thus the local heat flux vary significantly across the plated [34]. These measurements will be part of our future work.

ACKNOWLEDGMENTS

The authors wish to acknowledge the financial support by the Deutsche Forschungsgemeinschaft within the Research Unit FOR 1182, the Thüringer Ministerium für Bildung, Wissenschaft und Kultur as well as the China Scholarship Council (Grant No. 2009608062) for the work reported in this paper. Furthermore we thank V. Mitschunas, K. Henschel, and H. Hoppe for their technical assistance. Fruitful discussions with M. S. Emran and J. D. Scheel are also acknowledged.

[1] L. P. Kadanoff, Phys. Today **54**, 34 (2001).
[2] G. Ahlers, S. Grossmann, and D. Lohse, Rev. Mod. Phys. **81**, 503 (2009).
[3] R. du Puits, C. Resagk, A. Tilgner, F. H. Busse, and A. Thess, J. Fluid Mech. **572**, 231 (2007).
[4] M. S. Emran and J. Schumacher, J. Fluid Mech. **611**, 13 (2008).
[5] B. I. Shraiman and E. D. Siggia, Phys. Rev. A **42**, 3650 (1990).
[6] E. D. Siggia, Annu. Rev. Fluid Mech. **26**, 137 (1994).
[7] S. Grossmann and D. Lohse, J. Fluid Mech. **407**, 27 (2000).
[8] S. Grossmann and D. Lohse, Phys. Fluids **16**, 4462 (2004).
[9] H. Schlichting and K. Gersten, *Boundary Layer Theory* (Springer, Berlin, 2004).
[10] X. L. Qiu and P. Tong, Phys. Rev. E **64**, 036304 (2001).
[11] C. Sun, Y.-H. Cheung, and K.-Q. Xia, J. Fluid Mech. **605**, 79 (2008).
[12] Q. Zhou and K.-Q. Xia, Phys. Rev. Lett. **104**, 104301 (2010).
[13] R. du Puits, C. Resagk, and A. Thess, Phys. Rev. Lett. **99**, 234504 (2007).
[14] R. du Puits, C. Resagk, and A. Thess, Phys. Rev. E **75**, 016302 (2007).
[15] Q. Zhou, R. J. A. M. Stevens, K. Sugiyama, S. Grossmann, D. Lohse, and K.-Q. Xia, J. Fluid Mech. **664**, 297 (2010).
[16] R. J. A. M. Stevens, Q. Zhou, S. Grossmann, R. Verzicco, K.-Q. Xia, and D. Lohse, Phys. Rev. E **85**, 027301 (2012).
[17] Dantec User's Guide, 7-97 (2006).
[18] C. Resagk, R. du Puits, A. Thess, F. V. Dolzhansky, S. Grossmann, F. F. Araujo, and D. Lohse, Phys. Fluids **18**, 095105 (2006).
[19] R. Verzicco and P. Orlandi, J. Comput. Phys. **123**, 402 (1996).

[20] R. Verzicco and R. Camussi, J. Fluid Mech. **477**, 19 (2003).
[21] N. Shi, M. S. Emran, and J. Schumacher, J. Fluid Mech. **706**, 5 (2012).
[22] R. du Puits, C. Resagk, and A. Thess, Phys. Rev. E **80**, 036318 (2009).
[23] A. Belmonte, A. Tilgner, and A. Libchaber, Phys. Rev. E **50**, 269 (1994).
[24] S. L. Lui and K. Q. Xia, Phys. Rev. E **57**, 5494 (1998).
[25] J. D. Scheel, private communication (2011).
[26] R. Kaiser and R. du Puits, Exp. Fluids **53**, 137 (2012).
[27] E. Pohlhausen, Z. Angew. Math. Mech. **1**, 115 (1921).
[28] S. B. Pope, *Turbulent Flows*, 7th ed. (Cambridge University Press, Cambridge, 2010).
[29] Y. B. Xin, K. Q. Xia, and P. Tong, Phys. Rev. Lett. **77**, 1266 (1996).
[30] A. Tilgner, A. Belmonte, and A. Libchaber, Phys. Rev. E **47**, R2253 (1993).
[31] L. D. Landau and E. M. Lifschitz, *Fluid Mechanics*, 2nd ed. (Pergamon Press, New York, 1987).
[32] J. H. Preston, J. Fluid Mech. **3**, 373 (1958).
[33] X.-Z. He, D. Funfschilling, H. Nobach, E. Bodenschatz, and G. Ahlers, Phys. Rev. Lett. **108**, 024502 (2012).
[34] S. Wagner, O. Shishkina, and C. Wagner, J. Fluid Mech. **697**, 336 (2012).